Title: Hierarchical structured graphene/metal oxide/porous carbon composites as anode materials for lithium-ion batteries

Author: Rong Guo Wenbo Yue Yu Ren Wuzong Zhou

PII: S0025-5408(15)30093-3
DOI: http://dx.doi.org/doi:10.1016/j.materresbull.2015.08.027
Reference: MRB 8380

To appear in: *MRB*

Received date: 12-5-2015
Accepted date: 22-8-2015

Please cite this article as: Rong Guo, Wenbo Yue, Yu Ren, Wuzong Zhou, Hierarchical structured graphene/metal oxide/porous carbon composites as anode materials for lithium-ion batteries, Materials Research Bulletin http://dx.doi.org/10.1016/j.materresbull.2015.08.027

Hierarchical structured graphene/metal oxide/porous carbon composites as anode materials for lithium-ion batteries

Rong Guo [a], Wenbo Yue [a,*], Yu Ren [b], Wuzong Zhou [c]

[a] Beijing Key Laboratory of Energy Conversion and Storage Materials, College of Chemistry, Beijing Normal University, Beijing 100875, P. R. China

[b] National Institute of Clean-and-low-carbon Energy, Beijing 102209, P. R. China

[c] School of Chemistry, University of St. Andrews, St. Andrews, Fite KY16 9ST, United Kingdom

Graphical abstract

Research Highlights

- CeO_2 and Co_3O_4 nanoparticles display different behavior within CMK-3.
- CMK-3-CeO_2 and Co_3O_4 show various electrochemical properties.
- CMK-3-CeO_2 and Co_3O_4 are further wrapped by graphene nanosheets.
- Graphene-encapsulated composites show better electrochemical performances.

Abstract

As a novel anode material for lithium-ion batteries, CeO_2 displays imperceptible volumetric and morphological changes during the lithium insertion and extraction processes, and thereby exhibits good cycling stability. However, the low theoretical

* Corresponding author. Tel.: +86 10 58804229; Fax: +86 10 58802075.
E-mail address: wbyue@bnu.edu.cn (W.B. Yue)

capacity and poor electronic conductivity of CeO_2 hinder its practical application. In contrast, Co_3O_4 possesses high theoretical capacity, but undergoes huge volume change during cycling. To overcome these issues, CeO_2 and Co_3O_4 nanoparticles are formed inside the pores of CMK-3 and display various electrochemical behaviors due to the different morphological structures of CeO_2 and Co_3O_4 within CMK-3. Moreover, the graphene/metal oxide/CMK-3 composites with a hierarchical structure are then prepared and exhibit better electrochemical performances than metal oxides with or without CMK-3. This novel synthesis strategy is hopefully employed in the electrode materials design for Li-ion batteries or other energy conversion and storage devices.

Keywords: A. composites, B. chemical synthesis, D. electrochemical properties

1. Introduction

The demand for the energy storage and conversion devices is gradually increasing owing to the rapidly incremental global energy consumption. As one of the most important technologies for energy conversion and storage, lithium-ion batteries (LIBs) are widely used in portable electronic devices (e.g., cell phones) due to their outstanding advantages such as high energy density, long cycle life, no memory effect and environmental friendliness [1]. The selection of electrode materials is of great importance since the electrochemical performance of LIBs relies heavily on the electrode properties. Carbon-based materials (e.g., graphite) are usually used as anode materials for LIBs because of their low cost, high abundance and outstanding kinetics [2,3]. However, graphite suffers great danger from the formation of lithium dendrite during the overcharge process owing to its low Li-intercalation potential (0.2V vs.

Li/Li^+) [4]. Transition metal oxides are another one of the promising anode materials for LIBs and usually possess high theoretical capacities based on a redox mechanism. For instance, the theoretical capacity of Co_3O_4 is ~890 mA h g^{-1}, much higher than that of commercial graphite anode (372 mA h g^{-1}) [5-7]. But the severe volume change and poor electronic conductivity of Co_3O_4 during the charge and discharge processes may reduce its cycle and rate performances [8,9]. Recently, CeO_2 is reported as a novel LIB anode material and displays opposite electrochemical properties such as low theoretical capacity but imperceptible volumetric and morphological changes because of a fully reversible phase transformation between fluorite CeO_2 and cubic Ce_2O_3 during the electrochemical process [10-12]. In addition, the intrinsic low electronic conductivity of CeO_2 is also an impediment to its practical use for LIBs.

Carbon materials are usually used to support metal oxides in order to improve their electrochemical performances due to its high electronic conductivity. Moreover, porous carbon such as CMK-3 can further supply the improved electronic conducting network, buffers their volume variation during cycling, and hosts the nanosized metal oxide from aggregation and disintegration through its ordered mesopores [13-15]. Therefore, metal oxides-loaded porous carbons (e.g., CMK-3) ought to show better cycling stability and rate capability in principle. However, in our previous study and other relevant literatures, it has been found that the content of metal oxides in CMK-3-supported materials highly influences the electrochemical performances [16-18]. Namely, too high loading of metal oxides may destroy the mesostructure of CMK-3, and some large particles inevitably form outside the pores of CMK-3, leading to a capacity fading and poor cycle performance, whereas too low loading of metal oxides may reduce the theoretical capacities of the CMK-3-supported composites. Thus it is still a challenge to well

integrate metal oxides into porous carbon and avoid the formation of large particles outside the mesopores in order to pursue high-performance electrode materials for supercapacitors or LIBs.

Graphene, as a novel two-dimensional carbon nanosheet, has attracted many attentions due to its excellent properties such as large specific surface area, great mechanical strength, high electrical and thermal conductivity [19]. Accordingly, various graphene-based metal oxides are fabricated as a new class of advanced electrode materials with enhanced cycle and rate performances [20-23]. In the present work, CeO_2 and Co_3O_4 have been selected as functional guest materials to be loaded into CMK-3. One of the reasons of choosing them is the significantly different melting points of their precursors, which is a critical factor in the crystallization of oxides inside the template pores. Their structure, size and morphology have been revealed by electron microscopic studies. The apparent difference in the constructions of CMK-3-CeO_2 and CMK-3-Co_3O_4 (referred to as mC-CeO_2 and mC-Co_3O_4) influences their electrochemical performances. Furthermore, these CMK-3-supported metal oxides were further encapsulated by graphene nanosheets through the electrostatic interaction and hydrogen bonding. The hierarchical structure of graphene/metal oxide/porous carbon composites (referred to as G-mC-MOs, e.g., G-mC-CeO_2 and G-mC-Co_3O_4) may highly improve the electrochemical properties of the composite electrodes.

2. Experimental

2.1. Preparation of CMK-3-CeO_2 and CMK-3-Co_3O_4

CMK-3 was synthesized using sucrose as the precursor and SBA-15 as the template (see the Supporting Information) [24]. CMK-3-supported metal oxides were synthesized

by thermal decomposition of metal nitrates inside the pores of CMK-3. In a typical experiment, CMK-3 was first treated in nitric acid by ultrasonication for 0.5 h. Subsequently, 1.6 g of $Ce(NO_3)_3 \cdot 6H_2O$ or 2.2 g of $Co(NO_3)_2 \cdot 6H_2O$ was dissolved in 20 mL of ethanol, and then 0.5 g of CMK-3 was added into this solution. After stirring for 1 h, the ethanol was completely evaporated under vacuum at 60 °C. The dried powder was then heated to 200 °C with a constant heating rate of 2.5 °C min^{-1} and kept at that temperature for 2 h to obtain CMK-3-CeO_2 or CMK-3-Co_3O_4. For producing mesoporous metal oxides, the carbon template was removed by heating samples under an air atmosphere at 500 °C for 4 h.

2.2. Preparation of G-mC-CeO_2 and G-mC-Co_3O_4

Graphene oxide (GO) was synthesized from natural graphite powders by a modified Hummer's method (see the Supporting Information) [25]. Graphene-encapsulated CMK-3-metal oxides were synthesized by co-assembly of GO nanosheets and APTES (3-Triethoxysilylpropylamine) modified CMK-3-metal oxides [26]. In a typical experiment, 0.1 g of CMK-3-CeO_2 or CMK-3-Co_3O_4 was dispersed into 20 mL of n-hexane via sonication. After 30 min, 0.2 mL of APTES was poured into the above solution and refluxed for 12 h at 70 °C to obtain APTES-modified CMK-3-metal oxides. Subsequently, 0.01 g of GO and 0.04 g of APTES-modified CMK-3-metal oxides were dispersed in 80 mL of H_2O by ultrasonication for 0.5 h, respectively. The pH of GO solution was adjusted to ~8.0 with aqueous ammonia, and the pH of APTES-modified CMK-3-metal oxide suspension was adjusted to ~5.0 with dilute hydrochloric acid. Then the APTES-modified CMK-3-metal oxide suspension was added into the GO solution under mild magnetic stirring. After 1 h, the mixture was transferred into a

Teflon-lined stainless steel autoclave and maintained at 180 °C for 12 h. Finally, G-mC-CeO_2 or G-mC-Co_3O_4 was collected by centrifugation, washed with deionized water and dried at 60 °C.

2.3. Sample characterization

Specimens were initially characterized using XRD on a Phillips X'pert Pro MPD diffractometer with Cu K_α radiation. A Quantachrome NOVA 2000e sorption analyzer was used to examine the N_2 adsorption and desorption properties of specimens at liquid nitrogen temperature. The zeta-potentials of the GO, CMK-3-CeO_2 and APTES-modified CMK-3-CeO_2 suspensions were measured by a ZetaPlus zeta potential analyzer (Brookhaven Instruments Corporation). The Fourier transform infrared (FT-IR) spectra were recorded on a Nicolet-380 Fourier-transform infrared spectrometer in the range of 400-4000 cm^{-1}. X-ray photoelectron (XPS) spectra were recorded on a Shimadzu Axis Ultra spectrometer with an Mg K_α = 1253.6 eV excitation source. Raman scattering spectra were acquired by using a Jobin-Yvon Laser Confocal Micro-Raman Spectrometer with a 633 nm laser source. The thermogravimetric analysis (TGA) was performed on a NETZSCH STA 409 PC/PG thermal analyzer and carried out in air at a heating rate of 5 °C min^{-1}. Further characterization was performed by using transmission electron microscopy (TEM), high-resolution TEM (HRTEM) on a JEOL JEM-2011 electron microscope operated at 200 kV, scanning electron microscope (SEM) on a JEOL JSM-6700F electron microscope at an accelerating voltage of 1 kV.

2.4. Electrochemical measurements

For electrochemical characterization, the composite electrodes were fabricated by mixing the active materials, acetylene black and polyvinylidene difluoride (PVDF) dissolved in N-methyl-2-pyrrolidine (NMP) in a weight ratio of 80:10:10. The mixed slurry was pressed onto a copper foil and dried at 110 ℃ in vacuum for 24 h. Cell assembly was carried out in an Ar-filled glove box. The electrolyte was 1 M solution of $LiPF_6$ dissolved in a EC:DEC:DMC solution with a 1:1:1 volume ratio. Electrochemical performances were measured using a CR2032-type coin cell with lithium metal as the negative electrode. The galvanostatic charge–discharge performance was measured with a LAND test system at room temperature, and the voltage range was from 0.01 to 3.0 V (versus Li/Li^+), with a constant current of 0.1–2 A g^{-1}. Cyclic voltammetry tests were performed between 0.01 and 3.0 V with a scan rate of 0.5 mV s^{-1}, and the electrochemical impedance spectroscopy (EIS) was carried out in the frequency range from 100 kHz to 10 mHz on a Princeton PARSTAT 4000 electrochemical station.

3. Results and discussion

3.1. Morphology and structural characterization

Synthesis and characterization of CMK-3 is shown in **Fig. S1**, with a narrow pore size distribution at 3.6 nm. **Fig. 1A-D** show the SEM and TEM images of mC-CeO_2 and mC-Co_3O_4, respectively. It is confirmed that CMK-3, a negative replica of SBA-15, has a 3D pore system, and CeO_2 can crystallize inside the pores to form a 3D network, which can be seen as porous crystals when CMK-3 template is removed by the following thermal combustion (**Fig. 1E**). The average size of these porous spheres (referred to as m-CeO_2) is about 50 nm. Besides, these CeO_2 crystals extend to the outer surface of the CMK-3 particles (**Fig. 1A-B**). Although crystallization of Co_3O_4 also

took place inside the pores of CMK-3, the resultant nanocrystallites are separated as seen from the sample after removing the CMK-3 template (**Fig. 1F**, referred to as n-Co_3O_4). Except for these embedded nanocrystallites, some large Co3O4 particles formed on the outer surface of CMK-3 (**Fig. 1C-D**), consistent with previous reports [17,18]. The different morphological structures of CeO_2 and Co_3O_4 within CMK-3 may be attributed to the migration rate of molten precursors in the pores of CMK-3, which is a critical factor for the preparation of mesoporous metal oxides using CMK-3 as a template [27], and further systematic exploration would be worthwhile.

Bearing in mind that large particles/agglomerates are inevitably formed on the surface of CMK-3 when high loading of metal oxides is desired, and the mesostructure of CMK-3 may be partially destroyed during the Li-ion intercalation and deintercalation processes [17,18], we designed and synthesized G-mC-MOs by using a graphene film to protect the exposed particles, in order to preserve the mesostructure of porous carbon, and further enhance the electrical conductivity of the overall electrode. **Fig. 2A** shows the overall synthesis routes of G-mC-CeO_2 and G-mC-Co_3O_4. Since the isoelectric point of CeO_2 is slightly higher than that of graphene oxide (GO), the surface of CeO_2 nanospheres was modified by grafting of silane coupling agent KH550 to render the oxide surface positively charged (**Fig. 2B**). Subsequently, the modified mC-CeO_2 were assembled with negatively charged GO by their electrostatic interactions, and G-mC-CeO_2 was finally fabricated by reducing GO to graphene under hydrothermal treatment. **Fig. 2C** shows a SEM image of G-mC-CeO_2, revealing that mC-CeO_2 particles are well-wrapped by graphene nanosheets. The TEM image (**Fig. 2D**) also confirms the presence of transparent and wrinkled graphene nanosheets and the hierarchical structure of the G-mC-CeO_2 composites. The d-spacing of the lattice fringes in the HRTEM

image (**Fig. 2E**) is ~0.315 nm, corresponding to the (111) planes of the CeO_2 structure. Moreover, 3~4 layer graphene nanosheets with a lattice spacing of ~0.375 nm are also observed at the edge of G-mC-CeO_2, validating the effective graphene encapsulation.

The reduction degree of GO in composites may influence their electrochemical properties, and has been characterized by FT-IR, XPS and Raman spectroscopy. **Fig. 3A** shows the FT-IR spectra of GO and G-mC-CeO_2. The characteristic absorption bands in the spectrum of GO were assigned to the stretching vibrations of C–O at ~1084 cm−1, C–OH at ~1234 cm^{-1}, C=O at ~1730 cm^{-1}, and the skeletal vibration of C=C at ~1626 cm^{-1}. The bands around ~3412 and ~1383 cm^{-1} were assigned to the stretching and bending vibrations of O–H groups in GO and water molecules. In contrast, the C–O and C=O bands disappeared in the spectrum of G-mC-CeO_2, and the intensity of C–OH band decreased sharply, indicating that the oxygen-containing functional groups on the surface of GO were almost eliminated. Fig. 3B shows the survey XPS spectrum of G-mC-CeO_2, and only three elements (C, O and Ce) were detected. The Ce 3d XPS spectrum of G-mC-CeO_2 is shown in the inset of **Fig. 3B**. The $3d_{5/2}$ features at 882.9, 889.4 and 898.8 eV corresponded to V, V″ and V‴ components, respectively, while the $3d_{3/2}$ features at 901.5, 908.0 and 917.2 eV corresponded to U, U″ and U‴ components, respectively. The peaks corresponding to V′ and U′ were hardly detected, implying the presence of Ce^{4+} ion rather than Ce^{3+} ion in the composite [28]. **Fig. 3C** shows the C 1s XPS spectra of GO and G-mC-CeO_2. Four peaks centred at ca. 284.6, 286.6, 287.6 and 288.8 eV were observed in the spectrum of GO, corresponding to C–C, C–O, C=O and O–C=O groups, respectively [29]. In contrast, the intensities of these peaks related to the oxidized groups in the spectrum of G-mC-CeO_2 were much weaker than those in the spectrum of GO, suggesting the high

reduction of GO in the composite. The reduction of GO can be further supported by Raman characterization. Raman spectra of GO and G-H (pure GO treated under hydrothermal conditions) are shown in **Fig. 3D**. The D band around 1332 cm^{-1} was related to the vibration of sp^3 carbon atoms of disordered graphite, and the G band around 1578 cm^{-1} was related to the in-plane vibration of sp^2 carbon atoms in a 2D hexagonal lattice. The intensity ratio of the D band and G band (ID/IG) of G-H was 0.79, lower than that of GO (0.94), reflecting the formation of more sp^2 domains after hydrothermal reduction [30].

The morphology and structure of G-mC-Co_3O_4 composites were also elucidated by SEM and TEM. As shown in **Fig. 4A-B**, the flexible and ultrathin graphene nanosheets can be distinguished, and mC-Co_3O_4 particles as well as some individual Co_3O_4 agglomerates have been effectively protected by graphene nanosheets. The characteristic peaks in the XRD patterns of mC-CeO_2 and G-mC-CeO_2 (**Fig. 4C**) are indexed into the cubic CeO_2 structure (space group Fm-3m, a = 0.5412 nm), while both XRD patterns of mC-Co_3O_4 and G-mC-Co_3O_4 (**Fig. 4D**) show a crystalline phase of cubic Co_3O_4 (space group Fd-3m, a = 0.8110 nm), indicating that nitrates have been completely converted to the corresponding metal oxides in CMK-3. The XRD peak for GO at ~11° is absent in the XRD patterns of G-mC-CeO_2 and G-mC-Co_3O_4 due to the reduction of GO. Furthermore, the XRD peak for stacked graphene at around 26° was not detected, implying that the stacking of the graphene nanosheets was prevented due to the encapsulation. To compare the electrochemical behavior of CeO_2- and Co_3O_4-containing samples, the contents of CeO_2 and Co_3O_4 in the composites were controlled to be similar. The TGA curves (**Fig. 4E-F**) show that the contents of CeO_2 are ~57.3 wt

% for mC-CeO_2 and ~46.4 wt % for G-mC-CeO_2, while the contents of Co_3O_4 are ~57.8 wt % for mC-Co_3O_4 and ~47.1 wt % for G-mC-Co_3O_4.

3.2. Electrochemical performance

To investigate the effect of the novel hierarchical structure of G-mC-MOs on their electrochemical properties, the electrochemical performances of CeO_2- and Co_3O_4-containing composites were investigated by cyclic voltammetry and galvanostatic measurements. **Fig. 5A** shows the cyclic voltammograms (CV) of G-mC-CeO_2 in the 1st, 2nd, 3rd, and 6th cycles. In the first cathodic scan, the reduction peak at ~0.76 V corresponds to the reduction of CeO_2 to Ce_2O_3 and the formation of the solid electrolyte interphase (SEI) layer, while the reduction peak at ~0.08 V corresponds to the insertion of Li^+ into CMK-3/graphene. In the first anodic scan, two broad peaks are observed, indicating the corresponding reversible reaction. In the subsequent cycles, the reduction peak is slightly shifted and the CV curves almost overlap, reflecting a good reversibility. The first cycle charge–discharge voltage profiles for m-CeO_2, mC-CeO_2 and G-mC-CeO_2 at 0.1 A g^{-1} is also plotted (**Fig. 5B**). There is a flat plateau in the first-cycle discharge curve, in accordance with the CV result. Moreover, the first charge and discharge capacities dramatically increase with the introduction of CMK-3 and graphene, since the theoretical capacity of CeO_2 is not as high as that of Co_3O_4. More importantly, each CeO_2-containing sample exhibits good cycling stability and the capacities do not decrease after initial several cycles (**Fig. 5C**). After 100 cycles, the capacity of G-mC-CeO_2 maintained at ~550 mA h g^{-1} at 0.1 A g^{-1}, much higher than that of mC-CeO_2 (~360 mA h g^{-1}) or m-CeO_2 (~110 mA h g^{-1}), and any other previous reports [10-12]. G-mC-CeO_2 also has the best rate capability among these three samples

(**Fig. 5D**). For instance, the reversible capacity of G-mC-CeO_2 is ~260 mA h g^{-1} at 2 A g^{-1}, still higher than that of mC-CeO_2 (~140 mA h g^{-1}) or mC-CeO_2 (~50 mA h g^{-1}). Moreover, a capacity of ~560 mA h g^{-1} can be retained when the current density recovered to 0.1 A g^{-1}, also implying its good cycling stability.

In order to understand the superior performance of G-mC-CeO_2, the electrochemical impedance spectroscopy (EIS) measurements of these samples were performed after 3 cycles. The symbols of R_e, R_f, C_f, R_{ct}, C_d, and Z_w in the corresponding equivalent circuit model (**Fig. 5F**) denoted the electrolyte resistance, the resistance and capacitance of the SEI film, the charge transfer resistance, the double layer capacitance, and the Warburg impedance, respectively. The Nyquist plots of m-CeO_2, mC-CeO_2 and G-mC-CeO_2 (**Fig. 5E**) consist of two overlapping semicircles in the high and medium frequency range that reflects the migration of the Li^+ ions through the SEI film (R_f) and the charge transfer resistance (R_{ct}), and a sloping straight line in the low frequency range that reflected the diffusion properties of Li^+ ions in solid materials (Z_w). The diameter of the semicircle for G-mC-CeO_2 or mC-CeO_2 in the high–medium frequency region is much smaller than that of m-CeO_2, suggesting that the introduced CMK-3 and graphene can highly improve the electronic conductivity of the composite electrode, and thereby gave rise to the improved electrochemical performance in LIBs. The R_f and R_{ct} values of these samples are shown in **Table S1**.

Similar to the performances of CeO_2-containig samples, G-mC-Co_3O_4 exhibited better cycle and rate performances than mC-Co_3O_4 by virtue of the graphene encapsulation (**Fig. 6A-B**). Moreover, compared to CeO_2-containig samples, the reversible capacities of mC-Co_3O_4 and G-mC-Co_3O_4 at initial several cycles were much higher (800–900 mA h g^{-1}) owing to the high theoretical capacity of Co_3O_4.

Nevertheless, the capacity of G-mC-Co_3O_4 still decayed after 20 cycles. To deeply explore the difference in cycle performances, the morphologies of G-mC-CeO_2 and G-mC-Co_3O_4 after 100 cycles were characterized by SEM. The morphology of mC-CeO_2 particles could be preserved under graphene protection even after 100 cycles and CeO_2 nanospheres were also distinguished, whereas only particle agglomerates are demonstrated in the SEM image of G-mC-Co_3O_4 (**Fig. S2**). Apparently, the hierarchical structure of G-mC-Co_3O_4 cannot be maintained for the long cycling, and a possible explanation is put forward. First, CeO_2 nanospheres were formed around the nanorods of CMK-3 and the volume variation of CeO_2 can be accommodated by the pores of CMK-3, while in addition to nanoparticles inside the pores of CMK-3, some large Co_3O_4 particles/agglomerates were formed outside the pores of CMK-3. Second, the volume change of CeO_2 was not as large as that of Co_3O_4 during Li-ion intercalation and deintercalation processes. Third, mC-Co_3O_4 particles were not wrapped perfectly by graphene nanosheets because of the non-integrated mC-Co_3O_4. Therefore, the morphology of G-mC-CeO_2 rather than G-mC-Co_3O_4 can be maintained after 100 cycles, giving rise to a good cycleability. It is believed that the hierarchical structure of G-mC-CeO_2 (**Fig. S3**) is ideal for high-performance LIB and supercapacitor electrodes except for the low theoretical capacity of CeO_2.

The hierarchical structure of G-mC-MOs possesses several advantages: (1) nanosized metal oxide particles can be separated inside the pores of porous carbon, which provides free space to accommodate the volume expansion of metal oxides; (2) the exposed metal oxide particles can be protected by graphene nanosheets, which may also stabilize the mesostructure of porous carbon during cycles; and (3) both porous carbon and graphene can improve the electronic conductivity of the overall electrode. However, the

polarity difference between the nitrates and carbon may influence the migration of precursors inside the pores of porous carbon, and thereby results in many large particles formed on the surface of porous carbon, except for some lanthanide oxides which can be formed at a relatively low temperature. Other active materials with high theoretical capacities formed within porous carbon would be worthy of study in future.

4. Conclusions

Metal oxides (e.g., CeO_2 and Co_3O_4) showed completely different behavior inside the pores of CMK-3 because of various melting points of their precursors, leading to the selected formation of mesostructure after removal of CMK-3. Moreover, we designed a novel hierarchical structure of graphene/metal oxide/porous carbon composites, which not only limits the influence of volume variation of metal oxides, but also highly enhances the electronic conductivity of the electrode, thus leading to remarkable electrochemical behavior including high reversible capacity and good cycle/rate performance. It is noted that the different morphological structures of CeO_2 and Co_3O_4 within CMK-3 may highly influence their electrochemical performances, even after graphene encapsulation. We believe that this novel composite with hierarchical structure could be widely used in energy conversion and storage devices such as supercapacitors and batteries.

Acknowledgements

This work was financially supported by the Fundamental Research Funds for the Central Universities, and National Natural Science Foundation of China (21101014 and 21273022).

References

[1] H. Gwon, J. Hong, H. Kim, D.H. Seo, S. Jeon, K. Kang, Recent progress on flexible lithium rechargeable batteries, Energy Environ. Sci. 7 (2014) 538–551.

[2] X.Q. Yang, X.X. Li, Z.H. Li, G.Q. Zhang, D.C. Wu, Mesoporous wormholelike carbon with controllable nanostructure for lithium ion batteries application, Mater. Res. Bull. 66 (2015) 83–87.

[3] R. Guo, L. Zhao, W.B. Yue, Assembly of core–shell structured porous carbon–graphene composites as anode materials for lithium-ion batteries, Electrochim. Acta 152 (2015) 338–344.

[4] F. Chevallier, F. Poli, B. Montigny, M. Letellier, *In situ*^{7}Li nuclear magnetic resonance observation of the electrochemical intercalation of lithium in graphite: second cycle analysis, Carbon 61 (2013) 140–153.

[5] M.V. Reddy, G.V. Subba Rao, B.V.R. Chowdari, Metal oxides and oxysalts as anode materials for Li ion batteries, Chem. Rev. 113 (2013) 5364–5457.

[6] D.L. Wang, Y.C. Yu, H. He, J. Wang, W.D. Zhou, H.D. Abruna, Template-free synthesis of hollow-structured Co_3O_4 nanoparticles as high-performance anodes for lithium-ion batteries, ACS Nano 9 (2015) 1775–1781.

[7] Z.G. Fang, W.W. Xu, T. Huang, M.L. Li, W.R. Wang, Y.P. Liu, C.C. Mao, F.L. Meng, M.J. Wang, M.H. Cheng, A.S. Yu, X.H. Guo, Facile scalable synthesis of Co_3O_4/carbon nanotube hybrids as superior anode materials for lithium-ion batteries, Mater. Res. Bull. 48 (2013) 4419–4423.

[8] W.B. Yue, S.H. Jiang, W.J. Huang, Z.Q. Gao, J. Li, Y. Ren, X.H. Zhao, X.J. Yang, Sandwich-structural graphene-based metal oxides as anode materials for lithium-ion batteries, J. Mater. Chem. A 1 (2013) 6928–6933.

[9] Y.X. Yu, X.Y. Liu, X.H. Xia, Q.Q. Xiong, X.L. Wang, C.D. Gu, J.P. Tu, Net-structured Co_3O_4/C nanosheet array with enhanced electrochemical performance toward lithium storage, Mater. Res. Bull. 51 (2014) 112–118.

[10] C.X. Hua, X.P. Fang, Z.W.Yang, Y.R. Gao, Z.X. Wang, L.Q. Chen, Lithium storage mechanism and catalytic behavior of CeO_2, Electrochem. Commun. 25 (2012) 66–69.

[11] Q.M. Su, L. Chang, J. Zhang, G.H. Du, B.S. Xu, In situ TEM observation of the electrochemical process of individual CeO_2/graphene anode for lithium ion battery, J. Phys. Chem. C 117 (2013) 4292–4298.

[12] X.Y. Wu, H.L. Niu, S.S. Fu, J.M. Song, C.J. Mao, S.Y. Zhang, D.W. Zhang, C.L. Chen, Core–shell CeO_2@C nanospheres as enhanced anode materials for lithium ion batteries, J. Mater. Chem. A 2 (2014) 6790–6795.

[13] X.L. Ji, K.T. Lee, L.F. Nazar, A highly ordered nanostructured carbon–sulphur cathode for lithium–sulphur batteries, Nat. Mater. 8 (2009) 500–506.

[14] L.F. Shen, X.G. Zhang, E. Uchaker, C.Z. Yuan, G.Z. Cao, $Li_4Ti_5O_{12}$ Nanoparticles embedded in a mesoporous carbon matrix as a superior anode material for high rate lithium ion batteries, Adv. Energy Mater. 2 (2012) 691–698.

[15] S.J. Yang, S. Nam, T. Kim, J.H. Im, H. Jung, J.H. Kang, S. Wi, B. Park, C.R. Park, Preparation and exceptional lithium anodic performance of porous carbon-coated ZnO

quantum dots derived from a metal–organic framework, J. Am. Chem. Soc. 135 (2013) 7394–7397.

[16] H.J. Zhang, H.H. Tao, Y. Jiang, Z. Jiao, M.H. Wu, B. Zhao, Ordered CoO/CMK-3 nanocomposites as the anode materials for lithium-ion batteries, J. Power Sources 195 (2010) 2950–2955.

[17] S.S. Tao, W.B. Yue, M.Y. Zhong, Z.J. Chen, Y. Ren, Fabrication of graphene-encapsulated porous carbon-metal oxide composites as anode materials for lithium-ion batteries, ACS Appl. Mater. Interfaces 6 (2014) 6332–6339.

[18] R. Guo, W.B. Yue, Y.M. An, Y. Ren, X. Yan, Graphene-encapsulated porous carbon-ZnO composites as high-performance anode materials for Li-ion batteries, Electrochim. Acta 135 (2014) 161–167.

[19] A.K. Geim, K.S. Novoselov, The rise of graphene, Nat. Mater. 6 (2007) 183–191.

[20] W.B. Yue, S. Yang, Y.L. Liu, X.J. Yang, A facile synthesis of mesoporous graphene-tin composites as high-performance anodes for lithium-ion batteries, Mater. Res. Bull. 48 (2013) 1575–1580.

[21] S. Yang, W.B. Yue, J. Zhu, Y. Ren, X.J. Yang, Graphene-based mesoporous SnO_2 with enhanced electrochemical performance for lithium-ion batteries, Adv. Funct. Mater. 23 (2013) 3570–3576.

[22] W.W. Zhou, C.Y. Ding, X.T. Jia, Y. Tian, Q.T. Guan, G.W. Wen, Self-assembly of Fe_2O_3/reduced graphene oxide hydrogel for high Listorage, Mater. Res. Bull. 62 (2015) 19–23.

[23] S.M. Li, B. Wang, B. Li, J.H. Liu, M. Yu, X.Y. Wu, Self-assembly of 2D sandwich-structured $MnFe_2O_4$/graphene composites for high-performance lithium storage. Mater. Res. Bull. 61 (2015) 369–374.

[24] S. Jun, S.H. Joo, R. Ryoo, M. Kruk, M. Jaroniec, Z. Liu, T. Ohsuna, O. Terasaki, Synthesis of new, nanoporous carbon with hexagonally ordered mesostructure, J. Am. Chem. Soc. 122 (2000) 10712–10713.

[25] W.S. Hummers, R.E. Offeman, Preparation of graphitic oxide, J. Am. Chem. Soc. 80 (1958) 1339–1339.

[26] S.B. Yang, X.L. Feng, S. Ivanovici, K. Müllen, Fabrication of graphene-encapsulated oxide nanoparticles: Towards high-performance anode materials for lithium storage, Angew. Chem. Int. Ed. (2010) 8408–8411.

[27] J. Roggenbuck, H. Schäfer, T. Tsoncheva, C. Minchev, J. Hanss, M. Tiemann, Mesoporous CeO_2: Synthesis by nanocasting, characterisation and catalytic properties, Micropor. Mesopor. Mater. 101 (2007) 335–341.

[28] D.G. Cheng, M.B. Chong, F.Q. Chen, X.L. Zhan, XPS characterization of CeO_2 catalyst for hydrogenation of benzoic acid to benzaldehyde, Catal. Lett. 120 (2008) 82–85.

[29] L. Zhao, W.B. Yue, Y. Ren, Synthesis of graphene-encapsulated mesoporous In_2O_3 with different particle size for high-performance lithium storage, Electrochim. Acta 116 (2014) 31–38.

[30] L. Shang, T. Bian, B.H. Zhang, D.H. Zhang, L.Z. Wu, C.H. Tung, Y.D. Yin, T.R. Zhang, Graphene-supported ultrafine metal nanoparticles encapsulated by mesoporous

silica: robust catalysts for oxidation and reduction reactions, Angew. Chem. Int. Ed. 53 (2014) 250–254.

Figure Captions

Fig. 1. SEM and TEM images of CMK-3/oxide composites, (A, B) mC-CeO_2 and (C, D) mC-Co_3O_4. TEM images of the specimens after removing the CMK-3 template, (E) m-CeO_2 and (F) n-Co_3O_4.

Fig. 2. (A) Schematic illustration of the synthesis route for mC-CeO_2/Co_3O_4 and G-mC-CeO_2/Co_3O_4. (B) Zeta potentials of GO, mC-CeO_2 and mC-CeO_2-NH_2 in aqueous solution at different pH values. (C) SEM, (D) TEM, and (E) HRTEM images of G-mC-CeO_2.

Fig. 3. (A) FT-IR and (C) C 1s XPS spectra of GO and G-mC-CeO_2. (B) Survey XPS spectrum of G-mC-CeO_2. The inset is the Ce 3d XPS spectrum of G-mC-CeO_2. (D) Raman spectra of GO and G-H.

Fig. 4. (A) SEM and (B) TEM images of G-mC-Co_3O_4. XRD patterns and TGA curves of (C, E) mC-CeO_2, G-mC-CeO_2 and (D, F) mC-Co_3O_4, G-mC-Co_3O_4, respectively.

Fig. 5. (A) CV curves of G-mC-CeO_2. (B) Charge–discharge curves of m-CeO_2, mC-CeO_2 and G-mC-CeO_2 at 0.1 A g^{-1} for the first cycle. (C) Cycle and (D) rate performances of these samples at 0.1 A g^{-1} and 0.1–2 A g^{-1}. (E) Electrochemical impedance spectra of these samples after 3 cycles and (F) the equivalent circuit model.

Fig. 6. (A) Cycle and (B) rate performances of mC-Co_3O_4 and G-mC-Co_3O_4 at 0.1 A g^{-1} and 0.1–2 A g^{-1}.

Figures

Fig. 1.

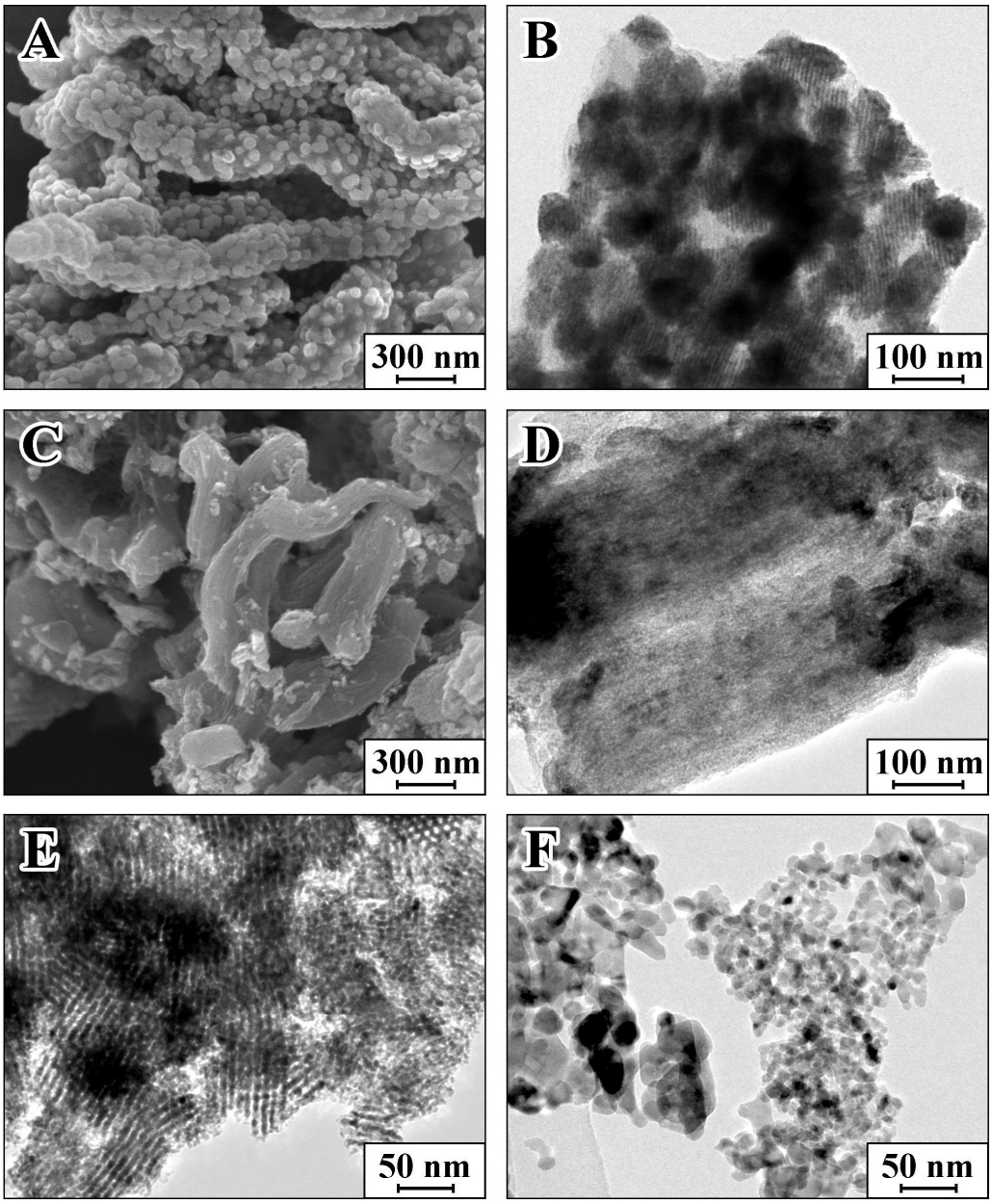

Fig. 2.

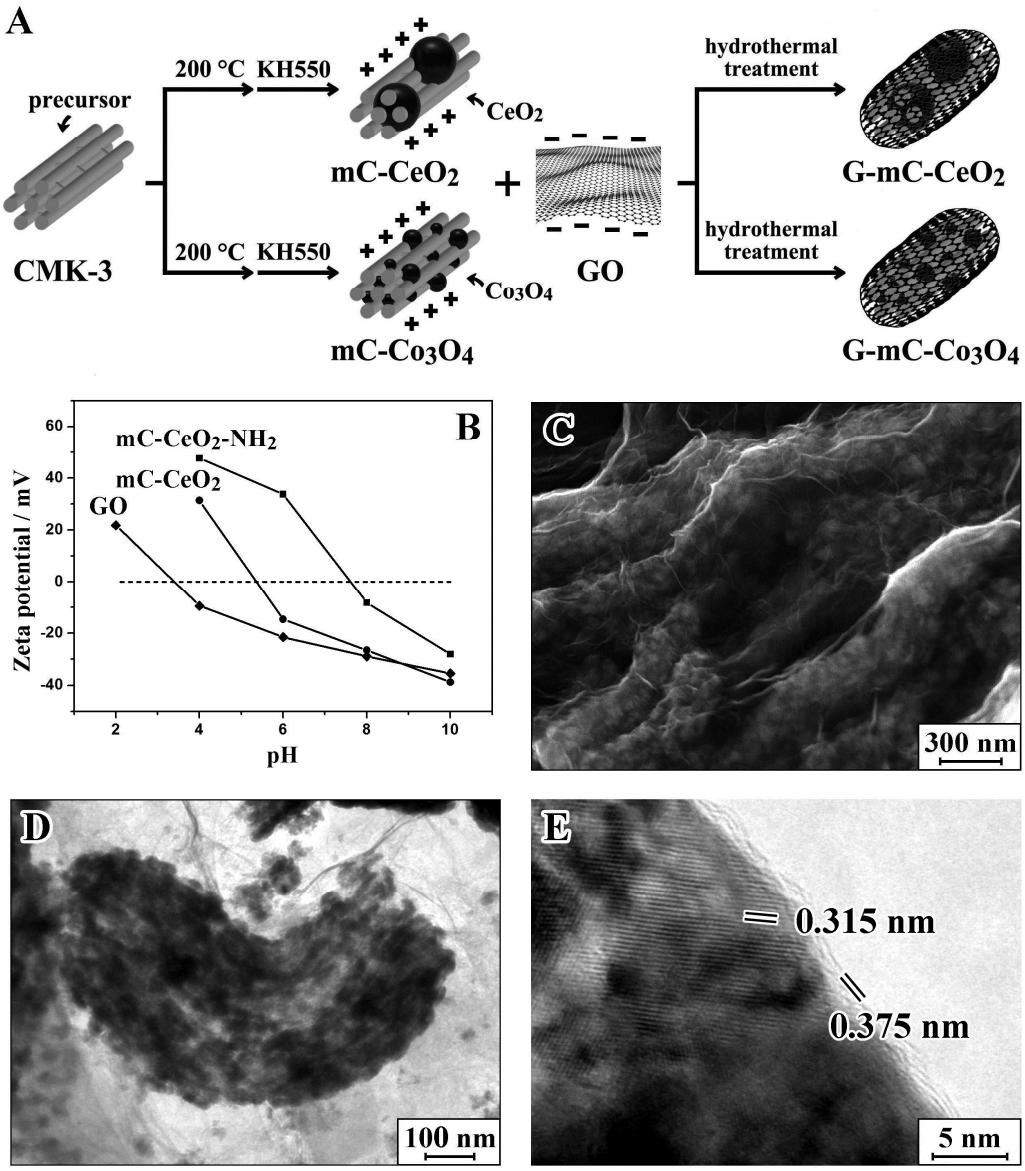

Fig. 3.

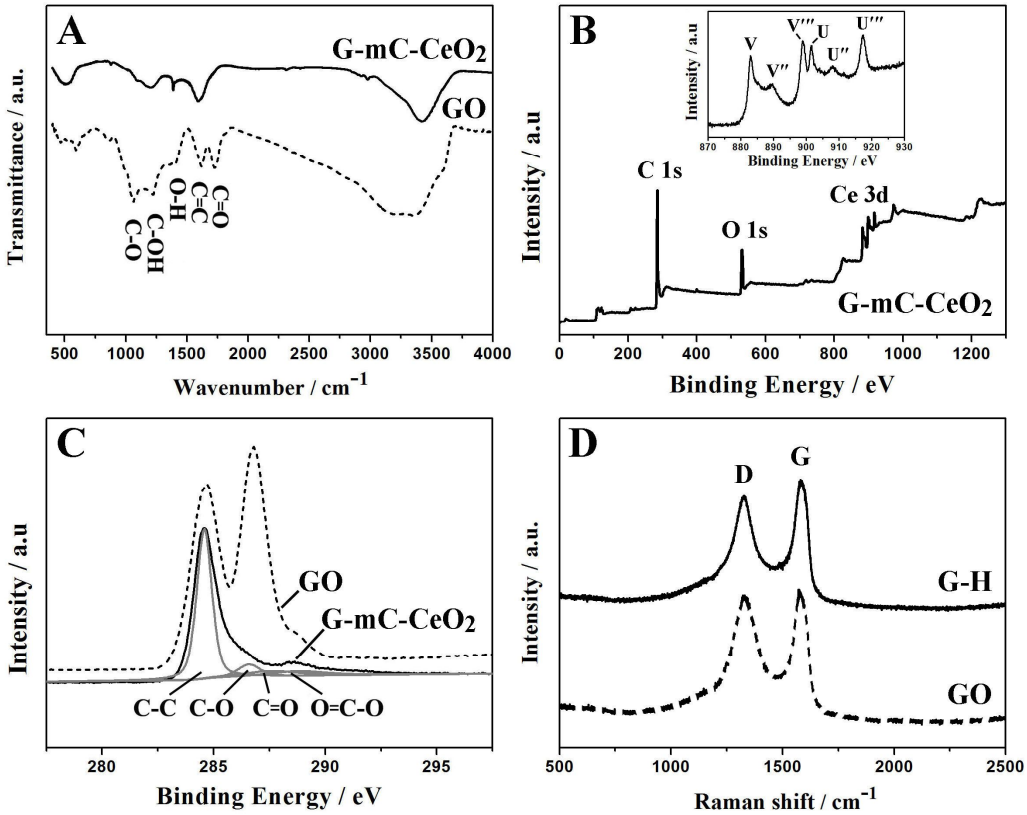

Fig. 4.

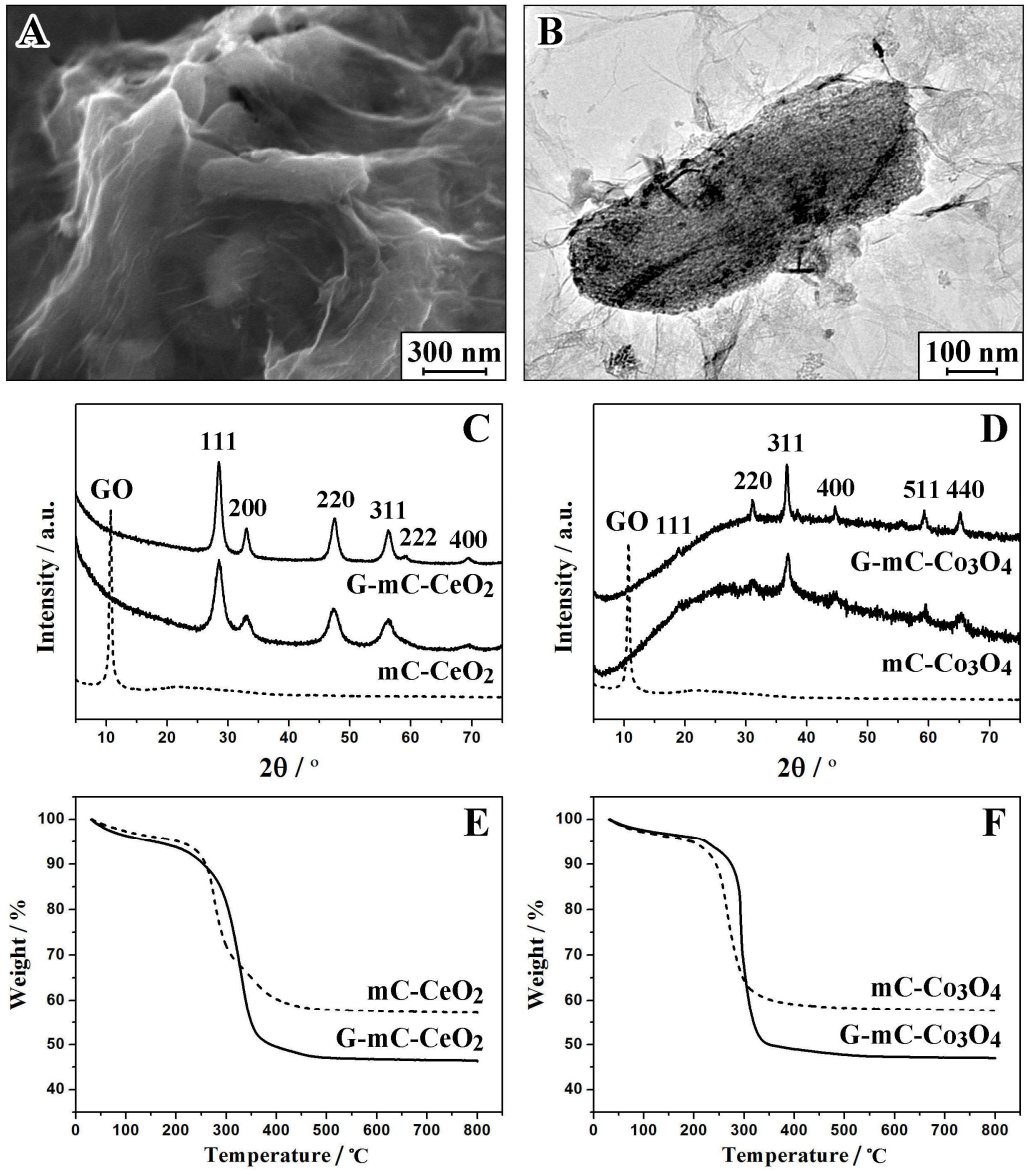

Fig. 5.

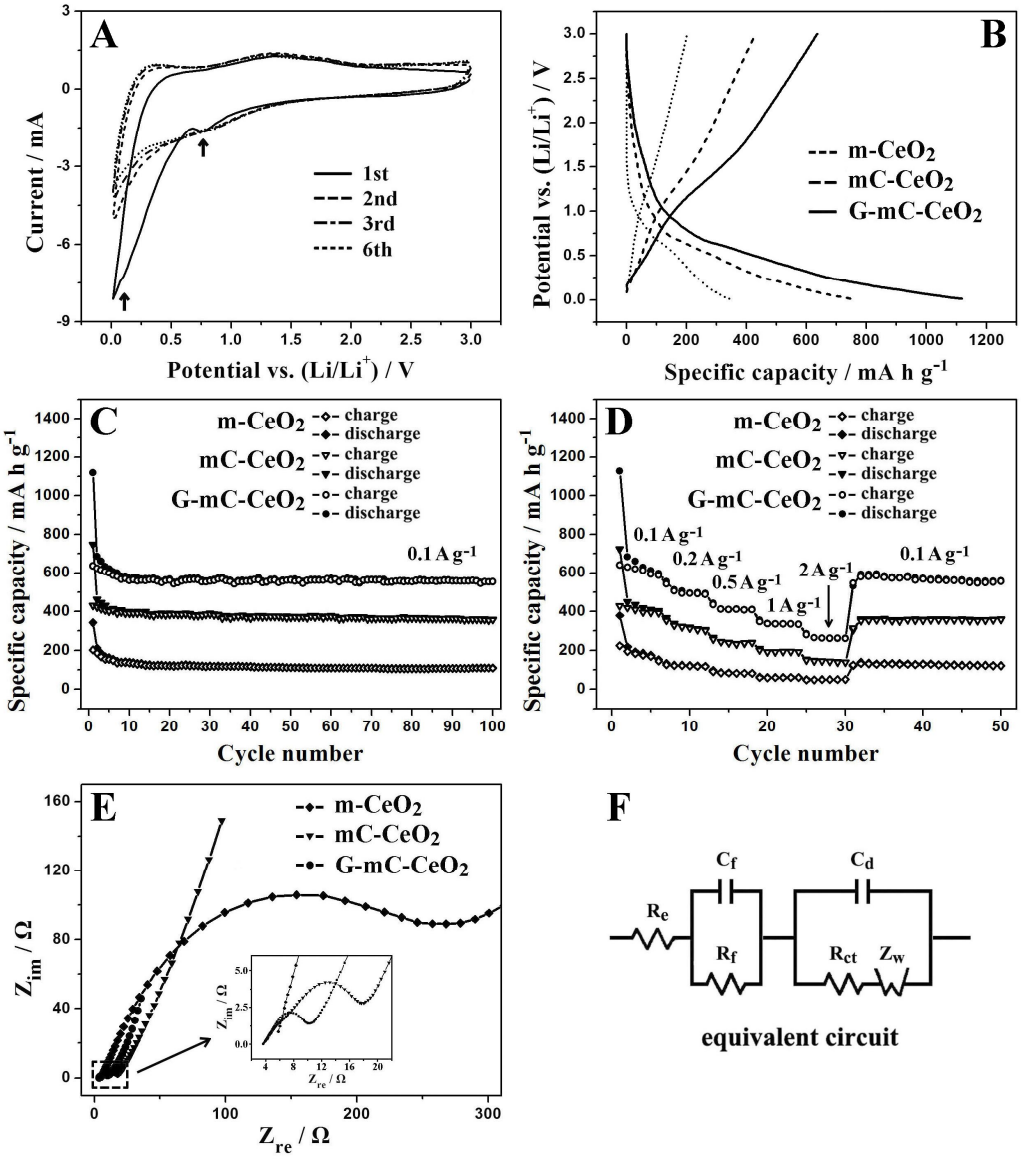

Fig. 6.